

Strain-Controllable High Curie Temperature and Magnetic Crystal Anisotropy in a 2D Ferromagnetic Semiconductive FeI₃ Monolayer

Zhaoyong Guan* and Shuang Ni

Cite This: *ACS Appl. Electron. Mater.* 2021, 3, 3147–3157

Read Online

ACCESS |



Metrics & More



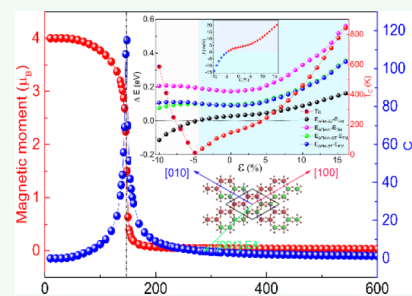
Article Recommendations



Supporting Information

ABSTRACT: The investigation of two-dimensional (2D) intrinsic ferromagnetic (FM) semiconductors (SCs) is a significant focal point in the field of spintronics. The FeI₃ monolayer (ML) with intrinsic ferromagnetism was fabricated by density functional theory and confirmed by a global minimum search. The FeI₃ ML is a half-semiconductor (HSC) with a band gap of 1.692 eV where FeI₃ shows FM order with a Curie temperature (T_c) of 148 K. It shows perpendicular magnetic anisotropy (PMA) and large magnetic anisotropy energy. Moreover, FeI₃ shows good dynamic and thermal stability. FeI₃ has a Young's modulus of 35.6 GPa, and biaxial strain could be applied to tune electronic and magnetic properties of FeI₃. The band gap, magnetic moment, magnetic exchange parameter (J), and T_c could be effectively controlled by the biaxial strains. It originates from the states near the Fermi-level coming from the contribution of the in-plane atomic orbitals. As the compressive strains increase, FeI₃ ML changes from the FM order with PMA into the antiferromagnetic (AFM) state with an in-plane magnetic anisotropy under larger compressive strains (-4.7%). The corresponding critical temperatures, including T_c and Néel temperature (T_N), are changed from 148 K (T_c) to 586 K (T_N , -10%). Additionally, FeI₃ ML changes from HSC to a normal spin-unpolarized SC under larger compressive strains ($\epsilon < -4.7\%$). As tensile strain increases, the energy difference between FM and AFM orders and J monotonously increase as the direct exchange interaction between Fe atoms weakens. The T_c values are also increased to 460 K (10%) and 842 K (16%). Also, FeI₃ ML remains HSC with the FM order. The magnetoelectric phase transitions in the strained FeI₃ appear, helping researchers to study the controllable magnetoelectric properties of FeI₃ in electronic and spintronic equipment.

KEYWORDS: high Curie temperature, magnetic crystal anisotropy, 2D ferromagnetic, FeI₃ monolayer, biaxial strains, mechanical properties, half-semiconductor



1. INTRODUCTION

Graphene has been synthesized *via* many methods¹ and has demonstrated many attractive physical properties.^{2,3} Other two-dimensional (2D) materials,^{4–6} such as hexagonal boron nitride,⁷ transition-metal dichalcogenides (TMDs),^{8–10} and black phosphorus,¹¹ show interesting and attractive properties.¹² Most 2D materials are nonmagnetic materials as long-range magnetic orders at a finite temperature in 2D materials is prohibited.¹³ As a result, 2D magnetic materials have only appeared in recent years,^{14–17} which show wide applications in the spintronics. In recent years, 2D van der Waals (vdW) materials,^{14–17} such as 2H-VSe₂,¹⁹ Cr₂Ge₂Te₆,^{20,21} CrI₃,^{15,16,22} Fe₃GeTe₂,¹⁸ with intrinsic magnetism have been synthesized and attracted much attention.^{16,23} Ferromagnetic (FM) Fe₃GeTe₂ has a T_c of 223 K,²⁴ while Fe₃GeTe₂ is a metal,²⁵ which restricts its application in the electronics. The T_c of 2H-VSe₂ is larger than 300 K,¹⁹ but the corresponding magnetic and electronic properties are modulated by the substrate.¹⁹ The Cr₂Ge₂Te₆ monolayer (ML) has a T_c of 220 K,²⁶ while it also displays metallicity.²⁷ In summary, magnetic semiconductors (SCs) are rare. Moreover, the T_c of the FM material is usually quite low and difficult to increase.

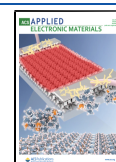
Therefore, these two obstacles prevent wide 2D materials' application in the spintronics.^{12,28} Enormous magnetic orders,^{22,29} various electronic properties,³⁰ high T_c ,³¹ and tunable magnetoelectric properties of SCs³² are the research hotspots in the field of 2D materials with intrinsic ferrimagnetism.^{22,28,31} In order to enlarge T_c and improve magnetic stability,⁴ researchers have modulated,^{23,24,32} synthesized,^{17,19} and designed magnetic SCs.^{4,31}

CrI₃ vdW structures have been successfully synthesized in previous works,^{16,33} and their magnetic orders are dependent on the layers and stacking orders.³⁴ Moreover, the corresponding T_c is much lower than room temperature.¹⁶ Therefore, many researchers have tried to increase T_c and control the magnetic and electronic properties of CrI₃.^{14,15,17,35–38} Strain can also be applied to tune CrI₃ from antiferromagnetic

Received: April 18, 2021

Accepted: June 21, 2021

Published: July 6, 2021



(AFM) to FM orders.^{37,39} Various vdW structures could be constructed from 2D materials and CrI₃,^{14–17,23,35,36,38} demonstrating interesting electronic,⁴⁰ magnetic,^{23,41} valley-tronic,⁴² and topological properties.⁴³ When the benzene molecule adsorbs on the CrI₃ ML, the corresponding T_c is increased to 65 K.⁴⁴ When hydrogen and oxygen adsorb on CrI₃, the corresponding T_c are 78 and 55 K, respectively.⁴⁵ Another strategy is replacing I atoms in CrI₃ with Cl or Br atoms, triggering a new phenomenon,^{46,47} where the corresponding T_c could be regulated ($T_c^{\text{CrBr}_3} = 41.3$ K, $T_c^{\text{CrCl}_3} = 29.7$ K).⁴⁶ However, this strategy is difficult to replicate. This leads us to consider how the properties of MI₃ (M = metal) change, when the Cr atom in CrI₃ is replaced with another transitional-metal (Fe) atom.

In this article, we performed a systematic study on the properties of FeI₃ by using density functional theory (DFT). The tunable intrinsic ferromagnetism in FeI₃ has a T_c of 148 K. FeI₃ is a half-semiconductor (HSC) with a gap of 1.692 eV under the intrinsic FM order, which originates from the superexchange interaction of the Fe and I atoms. The magnetic easy axis (EA) prefers to be perpendicular magnetic anisotropy (PMA), originating from indirect spin–orbital coupling (SOC). FeI₃ shows good dynamical and thermal stability. The Young's modulus of FeI₃ is 35.6 GPa, and the corresponding critical strain is 25%. The biaxial strain could effectively control the magnetic and electronic properties as the states near the Fermi-level are mainly contributed by the in-plane atomic orbitals. Our results indicate that iron (Fe) atoms ferromagnetically couple with each other under tensile and smaller compressive strains ($\epsilon < -4.7\%$). The ΔE initially decreases, which originates from the enhancement of direct exchange interaction between Fe and Fe atoms when the compressive strain increases. The magnetic exchange parameter (J) and T_c are described by Monte Carlo (MC) simulations. Also, they present a similar trend. Additionally, FeI₃ could be transferred from HSC to spin-unpolarized SC as the compressive strain increased owing to the enhancement of the direct exchange interaction. However, FeI₃ is still a HSC with FM order under tensile strains. The magnetic moment changes under strains for the different charge transfer. The magnetic moment initially increases before decreasing as the compressive strain increases. When the larger compressive strains ($\epsilon < -4.7\%$) are applied, the EA could be switched from the [001] direction to the [100] direction. EA remains out of plane under tensile strains. Our results provide controllable magnetoelectric properties of FeI₃, which is useful for the new magnetoelectric devices.

2. COMPUTATIONAL DETAILS

The calculation of FeI₃ was achieved with the plane-wave basis Vienna Ab initio Simulation Package (VASP) code⁴⁸ based on DFT. The generalized gradient approximation (GGA) with Perdew–Burke–Ernzerhof (PBE)⁴⁹ was adopted. There are Fe 3d electrons in FeI₃. Therefore, the strong-correlated correction need to be considered, and the hybrid Heyd–Scuseria–Ernzerhof (HSE06)^{50,51} functional and the GGA + U method⁵² were used to deal with this issue. The effective onsite Coulomb interaction parameter (U) and exchange interaction parameter (J_0) are set to 6.00 and 0.50 eV, respectively. The effective U_{eff} ($U - J_0$) was set to 5.50 eV to calculate magnetocrystalline anisotropy (MCA) energy and phonon spectra in addition to performing the molecular dynamics simulation. Moreover, the GGA + U method has an

effect on the lattice parameter, magnetic order, and MCA energy. More details can be found in Figure S1 in the Supporting Information. The vacuum space in the z -direction was set to 16 Å to avoid the virtual interactions between the images. The kinetic energy cutoffs for geometry optimization and energy calculations were set as 400 and 268 eV, respectively. The kinetic energy cutoff was set to be large enough to ensure the accuracy of calculation, and more discussions are provided in Figures S2 and S3 in the Supporting Information. All geometries are fully relaxed until the energy was converged to 10^{-6} eV, and the force was 1 meV/Å. $16 \times 16 \times 1$ Monkhorst–Pack k -grids were used for geometry optimization and $26 \times 26 \times 1$ for energy computation. There were weak vdW interactions. Therefore, the vdWs correction, DFT-D2 developed by Grimme,⁵³ was adopted. DFT-D2 was adopted.⁵ The SOC was considered in the band structure and MCA. Noncollinear non-self-consistent calculations were performed to evaluate total energies after self-consistent ground states are achieved. An energy cutoff of 420 eV is adopted to calculate the MCA energy. Also, a convergence of 1×10^{-8} eV is used for the calculation of the total energy. The corresponding k -grid was adopted $9 \times 9 \times 1$, without any symmetry constriction. The phonon spectra and the density of the states were calculated using the finite displacement method as implemented in Phonopy software.⁵⁴ A $4 \times 4 \times 1$ cell was adopted to calculate phonon spectra and the density of the state. The crisis of total energy and the Hellmann–Feynman force were 10^{-8} eV and 1 meV Å⁻¹, respectively. A total of 18 000 uniform k -points along high-symmetry lines were adopted to calculate phonon spectra. Ab initio molecular dynamics (AIMD) simulation was also performed to investigate geometrical stability. The constant moles–volume–temperature (NVT) ensemble with the Nosé–Hoover thermostat⁵⁵ was adopted. Also, the corresponding temperature is the room temperature of 300 K. The time step and total step are 1 fs and 10^4 , respectively. In AIMD simulation, a $2 \times 2 \times 1$ supercell was adopted. It was expected to dispel the effect of the periodic boundary conditions with a relatively smaller system size.

3. RESULTS AND DISCUSSION

3.1. Structure of FeI₃ ML. The structure of FeI₃ ML was fabricated and searched by particle swarm optimization (PSO).⁵⁶ The optimized lattice parameter is $a = b = 7.174$ Å, as shown in Figure 1a,b, which is little larger than that of CrI₃ (7.008 Å). The lattice parameter was obtained from fitting energies with different orders and strains, as shown in Figure 1c. The corresponding Fe–I bond was 2.798 Å, which is larger than that of CrI₃ of 2.717 Å. From the Bader analysis, about 1.15 e electrons were transferred from the Fe atom to the I atom with each I atom receiving 0.38 e electrons.⁵⁷

3.2. Magnetic Properties. The magnetic moment is mainly contributed by the Fe atom, and each Fe atom contributes 4.0 μ_B to the magnetic moment. The spin densities of FM and AFM orders are shown in Figure 2a–e, respectively. For both cases, spin orientations are initially in the off-plane direction. There are eight Fe atoms in the $2 \times 2 \times 1$ cell. Therefore, there is a 32.0 μ_B magnetic moment for the FM state in the supercell. There are four different AFM orders, including AFM–Néel (AFM–N), AFM–stripy (AFM–ST), AFM–zigzag (AFM–ZZ), and AFM–Néel-stripy (AFM–N-ST) orders. For the considered AFM orders, four ferromagnetically coupled Fe atoms contribute 16.0 μ_B , while the other four

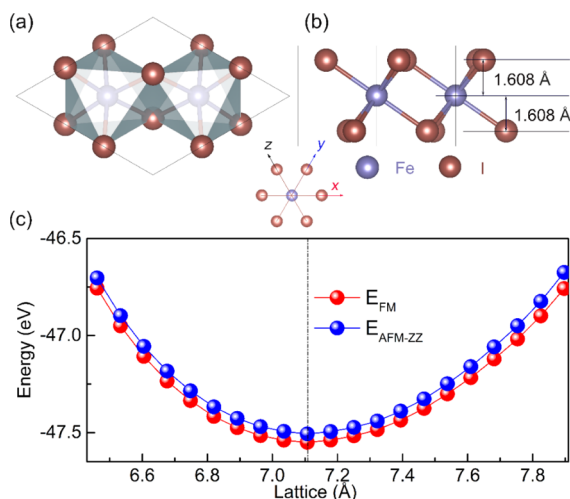


Figure 1. Optimized geometry of (a) top and (b) side views of FeI_3 ML. The blue and brown balls present Fe and I atoms, respectively. (c) Energies with FM and AFM-ZZ orders changing with the lattice parameters.

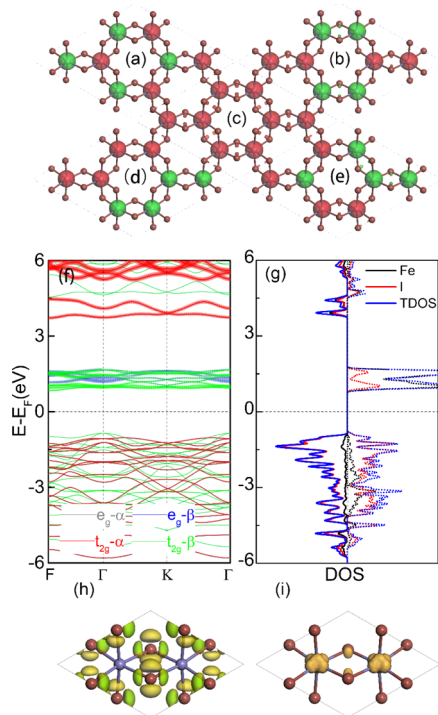


Figure 2. Top view of the optimized geometry of FeI_3 ML. The blue and brown balls represent Fe e_g (\uparrow , gray; \downarrow , blue) and Fe t_{2g} (\uparrow , red; \downarrow , green), respectively. (a–e) Spin charge densities of (a) AFM-N, (b) AFM-ST, (c) FM, (d) AFM-ZZ, and (e) AFM-S-ST orders of FeI_3 . The iso-value is 0.06 $\text{e}/\text{\AA}^3$. The red and green colors represent spin- α and spin- β electrons, respectively. (f) Spin-polarized band structure and (g) PDOS of FeI_3 ML; the solid and dashed lines represent projected band structures for Fe's spin- α and spin- β electrons, respectively. Charge densities of (h) VBM and (i) CBM. The iso-value is set to 0.75 $\text{e}/\text{\AA}^3$.

ferromagnetically coupled Fe atoms contribute $-16.0 \mu_B$ to the magnetic moment. Therefore, the total magnetic moment equals $0 \mu_B$. The corresponding spin densities are shown in Figure 2a–e. The corresponding energy differences between FM and AFM orders are defined as $\Delta E = E_{\text{AFM}} - E_{\text{FM}}$. The

$\Delta E_{\text{AFM-ZZ}}$ was defined as the energy difference between AFM-ZZ and FM orders ($\Delta E_{\text{AFM-ZZ}} = E_{\text{AFM-ZZ}} - E_{\text{FM}}$), resulting in a value of 0.028 eV. The energy differences between FM and other AFM orders such as $\Delta E_{\text{AFM-N}}$ ($\Delta E_{\text{AFM-N}} = E_{\text{AFM-N}} - E_{\text{FM}}$), $\Delta E_{\text{AFM-ST}}$ ($\Delta E_{\text{AFM-ST}} = E_{\text{AFM-ST}} - E_{\text{FM}}$), and $\Delta E_{\text{AFM-N-S}}$ ($\Delta E_{\text{AFM-N-S}} = E_{\text{AFM-N-S}} - E_{\text{FM}}$) were 0.174, 0.091, and 0.096 eV, respectively. The AFM-N order possessed the highest energy (-189.991 eV) when considering AFM orders, while the AFM-ZZ order (-190.137 eV) has the lowest energy in the AFM orders. AFM-N-ST and AFM-ST orders have energies of -190.069 and -190.074 eV, respectively. In fact, other orders such as noncollinear AFM orders have also been considered, but their energies are higher than that of FM orders. Therefore, FeI_3 ML is an intrinsic FM material.

Why does FeI_3 represent the FM order? In FeI_3 , each Fe is coordinated to six ligands-I, as shown in Figures 1 and 2a. The Fe d orbitals split into two parts: the threefold t_{2g} manifolds and twofold e_g manifolds for an octahedral crystal field. Moreover, the I–Fe–I bonding angle (90.259° , 95.597° , and 84.429°) was close to 90° , which explains the appearance of FM coupling according to the Goodenough–Kanamori–Anderson^{58–60} rules of the superexchange theorem. There is competition between FM and AFM coupling (origins from Fe–Fe direct exchange), similar to CrI_3 ML.⁶¹ The superexchange interaction was stronger than Fe–Fe direct exchange. Therefore, FeI_3 ML represents the FM ground state.

3.3. Electronic Structure. In the above section, the geometry and magnetic properties of FeI_3 were investigated, while the electronic properties were needed to be further investigated. The electronic properties were researched in this section; in addition, the band structure and the density of the state are shown in Figure 2f,g, respectively. The valence band maximum (VBM) occupied by the spin- β electron is located at the F-point of the first Brillouin zone (BZ). However, the conduction band minimum (CBM) composed of the spin- β electrons was located at the F-point of the first BZ. As a result, FeI_3 ML is HSC, with an indirect band gap of 1.692 eV calculated by the HSE06 functional. The gaps of spin- α ($E_{g-\alpha}$) and spin- β ($E_{g-\beta}$) channels are usually different in HSCs. The VBM of spin- α channel electrons is located at the point along high symmetric lines from the Γ -point to the K-point, while the CBM is located at the F-point. The VBM is mainly composed of I's p_x and p_y atomic orbitals, while the CBM is mainly contributed by Fe's d_{xz} atomic orbital, as shown in Figures 2 and S4, respectively. The states above the Fermi level are composed of d_{z^2} , d_{yz} , d_{xz} , d_{xy} , and $d_{x^2-y^2}$ atomic orbitals, as shown in Figure S5. The corresponding $E_{g-\alpha}$ equals 4.776 eV. The VBM of spin- β electrons is located at the Γ -point, while the CBM is located at the F-point. The corresponding $E_{g-\beta}$ was 1.692 eV. The band gap of the spin- α electron was 3.084 eV larger than that of the spin- β electron. As a result, spin- β electrons are more easily excited from the VB to the conduction band (CB), in comparison to spin- α electrons.

The band structures of FeI_3 with AFM orders were also calculated and were all classified as spin-unpolarized SCs, as shown in Figure S6. FeI_3 with AFM-N and AFM-ZZ orders was a normal spin-unpolarized SC with a direct gap of 1.892 eV, with the corresponding band structures shown in Figure S6a,d. For the AFM-N-ST and AFM-ST orders, the VBM was located at the K-point, while the CBM was located at the Γ -point. Therefore, FeI_3 with AFM-N-ST and AFM-ST orders were SCs with indirect gaps of 1.916 and 1.908 eV, respectively. The corresponding band structures are shown in

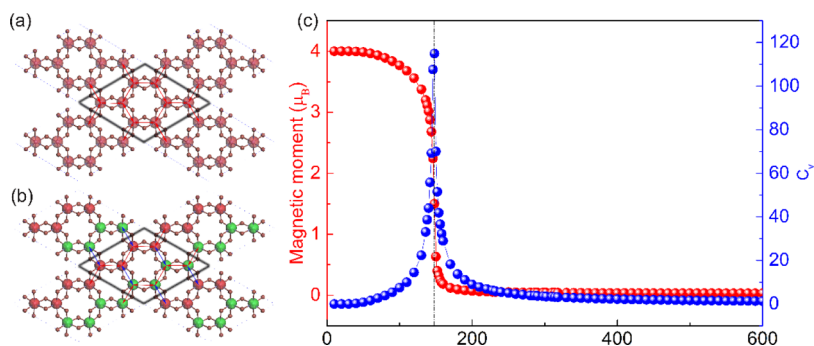


Figure 3. (a,b) Ising model showing the nearest exchange interactions. The spin densities of FeI_3 with (a) FM and (b) AFM-ZZ orders are shown. The red and green colors represent spin- α and spin- β electron densities, respectively. The red and blue arrows indicate Fe atoms and the nearest Fe atoms and are the FM and AFM interactions, respectively. The black diamond represents the supercell adopted in the simulation. (c) Magnetic moment per unit cell (red) and specific heat (C_v) (blue) varying with the temperature from classic Ising model MC simulation.

Figure S6b,c. In summary, the electronic properties of FeI_3 are related to the magnetic orders.^{3,31} FeI_3 with FM order is HSC, while FeI_3 is normal spin-unpolarized SC with AFM orders.

3.4. Curie Temperature. FM materials with high T_c are highly yearned. It was hoped that T_c would be large enough for use in desired applications. We adopt the classic Ising model to estimate J . The adopted magnetic configurations are shown in Figure 3, considering only the first-nearest neighbor interactions. The Hamiltonian can be written as

$$H = -J \sum_{\langle i,j \rangle} S_i \times S_j \quad (1)$$

$$E_{\text{FM}} = E_0 - \left(\frac{1}{2} \times 8 \times 3 \right) J |S|^2 \quad (2)$$

$$E_{\text{AFM}} = E_0 - 8 \times \left(-\frac{1}{2} \times 1 + \frac{1}{2} \times 1 \times 2 \right) J |S|^2 \quad (3)$$

$$J = \frac{E_{\text{AFM-ZZ}} - E_{\text{FM}}}{8|S|^2} \quad (4)$$

E_{FM} and $E_{\text{AFM-ZZ}}$ represent the energies of FM and AFM-ZZ orders, respectively. J and H represent the magnetic exchange parameter and Hamiltonian, respectively, and S_i represents the spin operator. Each Fe atom has $4.00 \mu_B$. The energies of the $(2 \times 2 \times 1)$ supercell with FM and AFM-ZZ orders were represented by eqs 2 and 3, respectively. The corresponding magnetic exchange parameter was $J = 3.55 \text{ meV}$, obtained with eq 4. In view of the disadvantage of the mean field theory,⁵ we used the classic Ising model MC simulations⁶² to estimate the magnetic moment as a function of temperature to calculate T_c . This MC code was developed by Xiang's group.⁶² Using this code, the estimated T_c of CrI_3 is about 51 K, which is consistent with the experimental value of 45 K.¹⁶ 6.0×10^6 loops with a 100×100 supercell was used in calculating T_c . The corresponding T_c is 148 K (shown in Figure 3), which is significantly larger than that of CrI_3 of 45 K.

3.5. Magnetocrystalline Anisotropy. For magnetic materials, when a magnetic moment is switched from EA to the hard axis, it costs energy.⁴ This energy is called magnetic anisotropy energy (MAE), which is used to overcome this "energy barrier".³¹ The MCA is defined as MAE per unit area. In our work, we aimed to achieve materials with high MCA and MAE.

For triangular systems, the energy at a certain direction (θ , ϕ) follows the following equations:⁶³

$$\Delta E_0 = K_1 \cos^2 \theta + K_2 \cos^4 \theta + K_3 \cos 3\phi \quad (5)$$

$$\Delta E_0 = E - E_0 \quad (6)$$

E represents the energy in a certain direction (θ , ϕ) with the polar angle θ and azimuthal angle ϕ , and E_0 is the global minimum energy. K_1 and K_2 represent the quadratic and quartic contributions to the energy. The energy difference ΔE_0 is independent of in-plane azimuthal angle ϕ , which implies $K_3 = 0$, as shown in Figure 4a. This conclusion could also be drawn from the symmetry (FeI_3 has the D_{3d} space group). Therefore, eq 5 is simplified into following equation:

$$\Delta E_0 = K_1 \cos^2 \theta + K_2 \cos^4 \theta \quad (7)$$

ΔE_0 equals 0 eV, when θ equals $\pi/2$, as shown in Figure 4b. E_0 reaches the maximum when the θ equals 0, indicating that EA is along the [001] direction. The energy difference (ΔE_0) changes as a function of the polar angle θ . The ΔE_0 is related to U_{eff} as MCA originates from the SOC, whose evaluated value is affected by U_{eff} . Additional tests can be found in Figure S9. MCAs with different U_{eff} s were calculated. The corresponding results are shown in Figure 4b. The MAE and MCA are affected by U_{eff} . When U_{eff} equals 5.5 eV, the corresponding ΔE_0 follows the quadratic equation $\Delta E_0 = 0.00268 \cos^2 \theta + 0.00052 \cos^4 \theta$. When U_{eff} equals 6.0 eV, ΔE_0 obeys the quadratic equation $\Delta E_0 = 0.00433 \cos^2 \theta + 0.00044 \cos^4 \theta$, as presented in Figure 4b. Therefore, the MAE and MCA could be evaluated with the following formulas:

$$\text{MAE} = E_{[100]} - E_{[001]} \quad (8)$$

$$\text{MCA} = E_{[100]} - E_{[001]} = \text{MAE}/S \quad (9)$$

$$S = a^2 \sin \frac{\pi}{3} \quad (10)$$

$E_{[100]}$ and $E_{[001]}$ represent the energies with the magnetic axis along the [100] and [001] directions, respectively. S is the area of the unit cell. When MAE and MCA are negative, it implies that EA is along the in-plane direction ([100]). The positive MAE and MCA indicate an out-of-plane preference for magnetization, as shown in Figure 4c. The MCA in 2D materials is larger than that of three-dimensional (3D) materials due to reduced dimensionality.⁷¹ FeI_3 is a 2D material, which is expected to be a sizable MCA. The MCA value can be estimated with SOC. The MAE and MCA values of FeI_3 ML were 3.19 meV and 1.15 erg/cm², respectively, when U_{eff} equals 5.5 eV. When U_{eff} is 6.0 eV, the MAE and

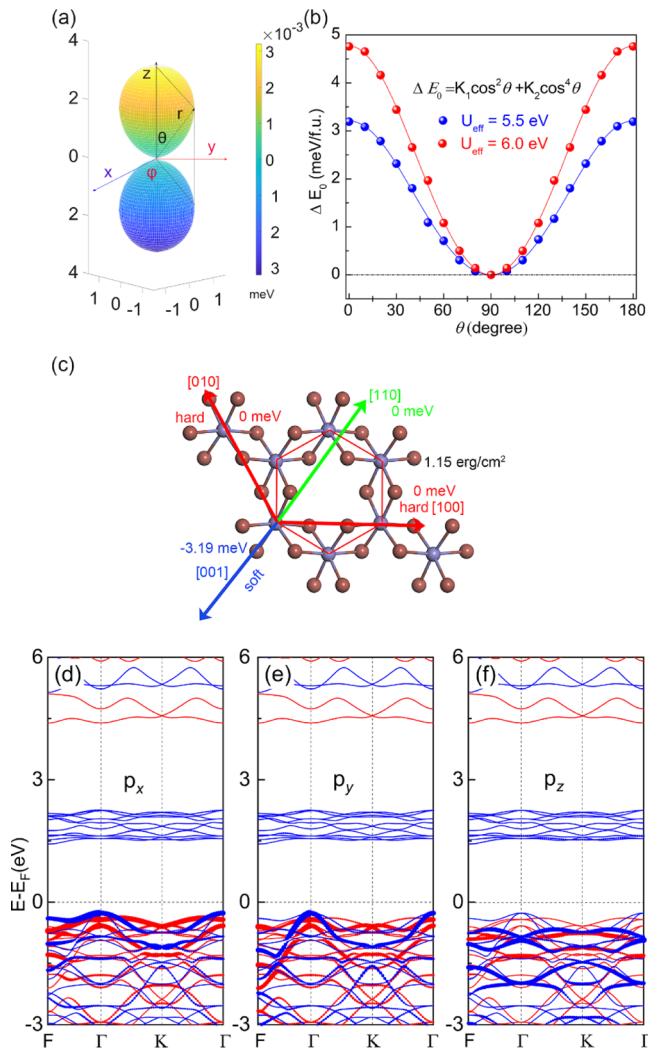


Figure 4. (a) MAE changes with θ and ϕ for FeI₃ ML. (b) Energy varies as a function of the polar angle θ of magnetization for FeI₃ ML. The MCA is calculated with the GGA + U method, and different colors present different ΔE . (c) Schematic of PMA. The figures represent the MAE and MCA, respectively. (d–f) I p orbital construction to the orbital angular momentum. (d) p_x , (e) p_y , and (f) p_z of I atomic orbitals projected the band structure. The red and blue lines represent spin- α and spin- β electrons, respectively.

MCA are 3.89 meV and 1.56 erg/cm², respectively, as shown in Figure S9. Our PBE + U calculations show that MAE (MCA) increases when the Hubbard U parameter is increased as the evaluated strength of SOC is affected by U . These values are larger than those of most known 2D magnets.⁶⁴

The MAE in FeI₃ ML is related to the spin and orbital structures near the Fermi level. In order to obtain a qualitative contribution of MAE, SOC is divided into two types: (i) a direct SOC term coupled with the orbital angular momentum states of Fe atoms and (ii) an indirect SOC term involved with the orbital angular momentum states of I atoms. Also, it is mediated by hopping between Fe and I atoms. The total SOC effect could be defined as $H_{\text{SOC}} = \xi_1 S^{\text{Fe}} \cdot L^{\text{Fe}} + \xi_2 S^{\text{Fe}} \cdot L^{\text{I}}$, where ξ_1 is the SOC constant in Fe atoms and ξ_2 represents effective (indirect) SOC between spins in Fe atoms and orbitals in I atoms. S^X and L^X are spin and orbital angular momentum operators for electronic states in X atoms, respectively. The indirect SOC makes the main contribution to the MAE, while

contribution of direct SOC is negligible by DFT.⁶⁵ When the indirect SOC contribution is taken into consideration, the perturbation theory⁶⁶ can be written as eq 11

$$\text{MAE} = \xi_1^2 \sum_{u,o,\sigma,\sigma'} \sigma\sigma' \frac{|\langle o, \sigma | L_z^{\text{Fe}} | u, \sigma \rangle|^2 - |\langle o, \sigma | L_x^{\text{Fe}} | u, \sigma \rangle|^2}{E_{u,\sigma} - E_{o,\sigma'}} + \xi_2^2 \sum_{u,o,\sigma,\sigma'} \sigma\sigma' \frac{|\langle o, \sigma | L_z^{\text{I}} | u, \sigma \rangle|^2 - |\langle o, \sigma | L_x^{\text{I}} | u, \sigma \rangle|^2}{E_{u,\sigma} - E_{o,\sigma'}} \quad (11)$$

Here, the first term and the second term represent the direct (Fe) and indirect (I) SOC contributions to the MAE and MCA, respectively. u and o represent the unoccupied and occupied states, respectively. $E_{u,\sigma}$ and $E_{o,\sigma'}$ are the band energies of the states. The spin indices σ and σ' run over ± 1 . The orbital angular momentum mainly comes from I atoms' contribution, as shown in Figure 4. Therefore, the first term in eq 11 was deemed to be negligible. Therefore, eq 11 was simplified into following equation:

$$\text{MAE} = \xi_2^2 \sum_{u,o,\sigma,\sigma'} \sigma\sigma' \frac{|\langle o, \sigma | L_z^{\text{I}} | u, \sigma \rangle|^2 - |\langle o, \sigma | L_x^{\text{I}} | u, \sigma \rangle|^2}{E_{u,\sigma} - E_{o,\sigma'}} \quad (12)$$

The orbital angular momentum, as shown in Figures 2g and 4d, mainly comes from the contribution of I atoms. The L_z operator can mix the two highest valence bands (VBs) and lowest conducting bands, substantially, leading to a sizable value of the matrix element $\langle o, \sigma | L_z | u, \sigma \rangle$. This results in $|\langle o, \sigma | L_z | u, \sigma \rangle|^2 - |\langle o, \sigma | L_x | u, \sigma \rangle|^2 > 0$ as the numerator. Our argument was confirmed by the DFT calculations: $\langle L_x \rangle, \langle L_y \rangle \gg \langle L_z \rangle$, as shown in Figure 4d–f. In order to clarify this contribution of orbital angular momentum, the relative spin polarization (σ, σ') of the states near the Fermi level is analyzed. The dominant contribution originates from the two VBs, which have opposite spin directions ($\sigma\sigma' = -1$) (Figure 4). Therefore, MAE is positive, favoring PMA.

3.6. Mechanical Properties. The mechanical properties of FeI₃ were also investigated. For lower stress, the relationship between stress and strain ($\sigma - \epsilon$) is represented by Hook's law. For a 2D hexagonal crystal, Hook's law can be expressed as

$$\begin{pmatrix} \sigma_{11} \\ \sigma_{22} \\ \sigma_{33} \end{pmatrix} = \begin{pmatrix} C_{11} & C_{21} & 0 \\ C_{12} & C_{22} & 0 \\ 0 & 0 & C_{66} \end{pmatrix} \begin{pmatrix} \epsilon_{11} \\ \epsilon_{22} \\ 2\epsilon_{12} \end{pmatrix} \quad (13)$$

where C_{11} , C_{22} , C_{12} , C_{21} , and C_{66} are the elastic stiffness constants, defined as

$$C_{11} = C_{22} = \frac{1}{A_0} \frac{\partial E_s}{\partial \epsilon_{11}^2}, \quad C_{12} = C_{21} = \frac{1}{A_0} \frac{\partial^2 E_s}{\partial \epsilon_{11} \partial \epsilon_{22}}, \quad C_{66} = \frac{1}{A_0} \frac{\partial^2 E_s}{\partial \epsilon_{12}^2} \quad (14)$$

Here, A_0 is the equilibrium area and E_s is the strained energy. Young's modulus $E(\theta)$ is evaluated with following equation:⁶⁷

$$E(\theta) = \frac{Y_{zz}}{\cos^4 \theta + d_2 \cos^2 \theta \sin^2 \theta + d_3 \sin^4 \theta} \quad (15)$$

$$d_1 = \frac{C_{11}}{C_{22}} + 1 - \frac{C_{11}C_{22} - C_{12}^2}{C_{22}C_{66}} \quad (16)$$

$$d_2 = -\left(2\frac{C_{12}}{C_{22}} - \frac{C_{11}C_{22} - C_{12}^2}{C_{22}C_{66}}\right) \quad (17)$$

$$d_3 = \frac{C_{11}}{C_{22}} \quad (18)$$

$$Y_{zz} = \frac{C_{11}C_{22} - C_{12}^2}{C_{22}} \quad (19)$$

As FeI₃ has a D_{3v} point group, $\theta = 0$. Therefore, the E could be expressed as

$$E(\theta) = Y_{zz} = \frac{C_{11}C_{22} - C_{12}^2}{C_{22}} \quad (20)$$

The corresponding Young's modulus of FeI₃ is 35.6 GPa, which is similar to that of CrI₃ (36 GPa).⁶⁸ Compared to graphene (1 TPa) and MoS₂ (270 GPa),⁶⁹ FeI₃ ML is quite "soft". Therefore, the biaxial strain should be more easily applied to FeI₃, compared with graphene and MoS₂. For "harder" TMD, thin films can even sustain strain up to about 11%.⁶⁹ Therefore, the much "softer" FeI₃ is expected to be much easier to applied larger strain (up to 16%).

The breaking and ideal strength are also evaluated with the relationship between strain energy ($E_s' = E' - E_0'$) and strain. The relationship between E_s' and ε is shown in Figure 5a. The

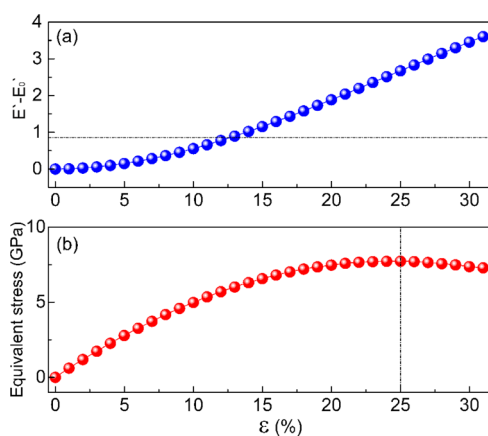


Figure 5. (a) Strained energies vary with biaxial strains. (b) Strain–stress relationship for FeI₃. The vertical dashed line presents critical strain and ideal strength, respectively.

stress–strain relationship for FeI₃ is shown in Figure 5b, and tensile strain ranges from 0 to 31%. For tensile strain, the relationship between applied strain and the corresponding tensile stress follows this equation

$$\sigma_{\text{tensile}} = \frac{1}{V(\varepsilon)} \frac{dE}{d\varepsilon} \quad (21)$$

The critical strain (ε_{max}) is 25%, and the corresponding ideal strength is 7.71 GPa. There is no plunge in the curve. Therefore, the applied biaxial strain (16%) is less than the

critical strength. In summary, FeI₃ ML can bear at least of 30% biaxial tensile strain. The phonon instability may occur before mechanical failure. The phonon band structure with applied biaxial strains was also calculated to check the dynamic stability. When the biaxial strain reaches 25%, an imaginary frequency appears.

The out-of-plane deformation induced by gravity could be estimated by the elastic theory in the following equation:⁷⁰

$$\frac{h}{L} = \sqrt[3]{\frac{\rho g L}{Y}} \quad (22)$$

where L is the length of the flake, set to 100 μm , and ρ is the areal density. It was found that $h/L = 5.2 \times 10^{-4}$. This value has the same order of magnitude as graphene flakes of the same size.⁷⁰ It implies that FeI₃ ML could withstand the weight and maintain a sandwich-like structure without obvious distortion.

3.7. Dynamical and Thermal Stability. The dynamical stability of FeI₃ was confirmed via phonon dispersion curves and the phonon density of the states. Also, they displayed no obvious imaginary phonon modes. The highest vibration frequency was evaluated to be 5.81 THz, as shown in Figure 6a, which is higher than that of ML CrI₃ (7.32 THz) but lower

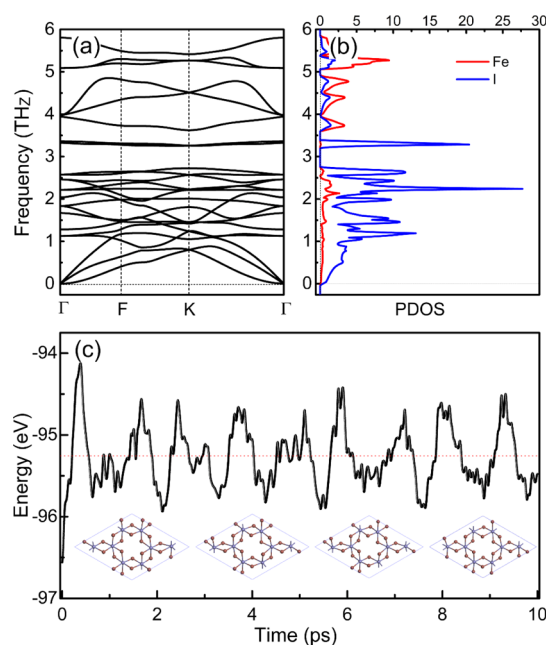


Figure 6. (a) Phonon spectrum and (b) density of the state of FeI₃ ML. The red and blue lines represent Fe and I atom projected phonon DOS, respectively. (c) Evaluation of energy with AIMD is calculated with the PBE + U method for 10 ps at 300 K. The red line represents total energies. The inset shows the atomic structure snapshots at certain times ($N = 2000, 4000, 8000, 10,000$) from AIMD.

than that of CrCl₃ (10.94 THz), as shown in Figure S10. Also, these values are related with the mechanical robustness of covalent bonds. It was found that I atoms make the main contribution for the low frequency ($0 < \varepsilon < 3.5$ THz), as shown in Figure 6b. On the contrary, Fe atoms make the main contribution for the high frequency ($3.5 < \varepsilon < 5.8$ THz). As a result, this affects the heat-transfer properties. Compared with the I atom (atomic weight: 126.9), the Fe atom (55.85) is lighter. As a result, the Fe atom makes the main contribution

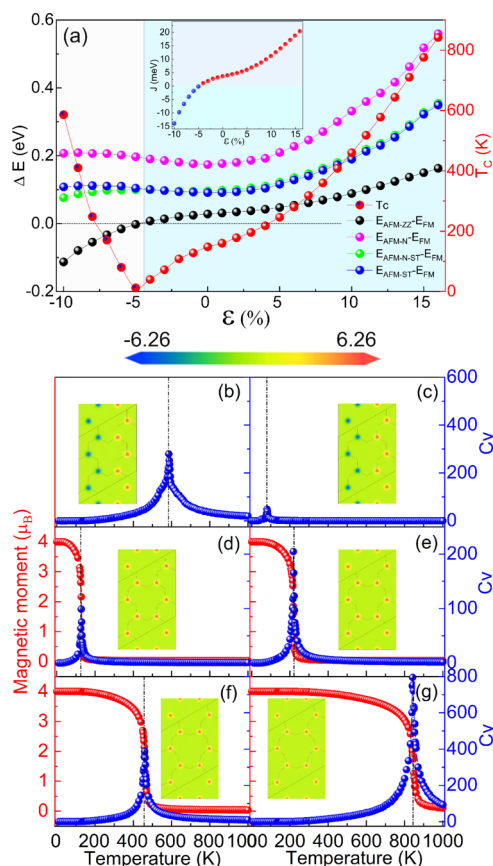


Figure 8. (a) $E_{AFM-ZZ} - E_{FM}$, $E_{AFM-N} - E_{FM}$, $E_{AFM-N-ST} - E_{FM}$, and $E_{AFM-ST} - E_{FM}$ represent the energy difference between AFM-ZZ, AFM-N, AFM-N-ST, and AFM-ST and FM orders, respectively. (b–g) Magnetic moment per unit cell (red) and C_v (blue) follow the change of the temperature from the MC simulation under biaxial strains of (b) $\epsilon = -10\%$, (c) $\epsilon = -6\%$, (d) $\epsilon = -1\%$, (e) $\epsilon = 4\%$, (f) $\epsilon = 10\%$, and (g) $\epsilon = 16\%$. The inset of (a) shows that the magnetic exchange parameter changes with the biaxial strains.

5.28, and 6.80 meV, as shown in the inset of Figure 8a. The corresponding T_c values were 178, 218, and 286 K, respectively. When the compressive strains were further increased, the ΔE further increased to 69.38 (8%), 88.85 (10%), 111.61 (12%), and 137.02 (14%) meV, and the J values were 8.67, 11.11, 13.95, and 17.13 meV, respectively. Meanwhile, the corresponding T_c also increased to 360, 460, 578, and 710 K, as shown in Figure 7b–f. Moreover, other AFM orders, such as AFM-N, AFM-ST, and AFM-N-S, were also weakened with increases in tensile strain, as shown in Figure 8a. The ΔE_{AFM-N} , ΔE_{AFM-ST} , and $\Delta E_{AFM-N-S}$ also increased as the biaxial strain increased, while the AFM-ZZ order possessed the lowest energy in consideration to the AFM orders.

The biaxial strain tunes the charge transfer between Fe and I atoms. Therefore, the magnetic moment of Fe atoms varies with the biaxial strains. When smaller compressive strains such as $\epsilon = -2, -4\%$ are applied, the corresponding magnetic moments of each Fe atom are 3.883 and 3.882 μ_B , respectively. As the compressive strain equals -4.7% , there is a phase transition from the FM order to the AFM order. The Fe atoms have a magnetic moment of 3.879 μ_B ($-3.879 \mu_B$). As the compressive strain goes on increasing ($\epsilon = -5, -7, -9\%$), the corresponding magnetic moments are 3.879, 3.869, and 3.854

μ_B , respectively. The spin densities are shown in Figure 8. When the compressive biaxial strains are further increased to -10% , the magnetic moment is 3.845 μ_B . The total magnetic moment is 0, and the corresponding spin density is shown in Figure 8b. The magnetic moment decreases under larger compressive strains.

When the tensile strains are applied to FeI₃, the magnetic moment stepwise decreases. For the smaller tensile strains ($\epsilon = 1, 3, 5\%$), the corresponding magnetic moments are 3.882, 3.878, and 3.872 μ_B , respectively. As the larger tensile strains ($\epsilon = 6, 8, 10\%$) are applied to FeI₃, the corresponding magnetic moments are 3.868, 3.858, and 3.847 μ_B , respectively. When the tensile strain goes on increasing, the corresponding magnetic moments are 3.840 (11%), 3.825 (13%), and 3.798 μ_B (16%), respectively. The spin densities of FeI₃ are represented in the insets of Figure 8f,g. A similar trend also appears in CrI₃, which originates from the change of charge transfer between Fe and I atoms.³⁹

In conclusion, as the d_{Fe-Fe} gets bigger, the tensile strain also increases. The corresponding ΔE , J , and T_c values increase as the AFM direct exchange interaction between the Fe atoms weakens. When the compressive strains were applied to FeI₃, the d_{Fe-Fe} were reduced. As a result, ΔE , J , and T_c values decrease as the direct exchange interaction is enhanced.

3.10. MCA Modulation. The MCA results from SOC and the strains were capable of controlling the strength of SOC by changing the bonding characteristics. Therefore, MAE and MCA could be affected by the biaxial strains. As the tensile strain increases, the MAE monotonically increases. The MCA energies were increased to 1.425 ($\epsilon = 1\%$) and 1.663 erg/cm² ($\epsilon = 2\%$). As ϵ continued to increase to 6 and 8%, the MCA was increased to 3.441 and 5.741, erg/cm², respectively. For larger tensile strains such as $\epsilon = 10, 12, 14$, and 15%, the corresponding MCA energies equal to 10.098, 17.153, 26.511, and 33.061 erg/cm², respectively, as shown in Figure 9. When ϵ was increased to 16%, the MCA energy was as high as 38.435 erg/cm².

As the compressive strain increased to $-2, -4$, and -4.5% , the corresponding MCA energies decreased to 0.661, 0.167, and 0.051 erg/cm², respectively. When the ϵ approached -4.7% , the MCA energy was -0.005 erg/cm². The MCA

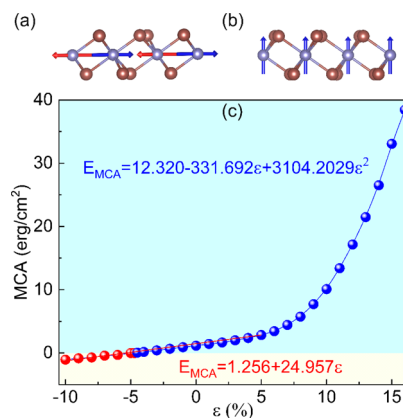


Figure 9. Optimized structure of FeI₃ ML with (a) PMA and (b) in-plane magnetic anisotropy. Red and blue lines represent different spin orientations. (c) MCA energy changes with ϵ . The blue and yellow areas represent positive and negative MCA energies, respectively. The blue and red lines with balls represent that EA is along the [001] and [100] directions, respectively.

energy changed from positive to negative, indicating that EA switched from in-plane [100] to out-of-plane [001]. This originates from the change of the indirect SOC. As the compressive strain continued to increase, the MCA was further enhanced. The corresponding values were -0.006 (-5%), -0.420 (-7%), and -0.833 erg/cm² (-9%). When the ε was increased to -10% , the MCA energy was -1.048 erg/cm². For smaller strains ($-10\% < \varepsilon < 5\%$), the MCA energy and ε followed a linear relationship: $E_{\text{MCA}} = 1.256 + 24.957\varepsilon$. When the strain was larger than 5% , the MCA energy and ε followed the quadratic function $E_{\text{MCA}} = 12.320 - 331.692\varepsilon + 3104.203\varepsilon^2$. This may stem from the obvious enhancement of the indirect SOC as the larger tensile ε increased. In summary, the biaxial strain was able to tune MAE and MCA by controlling the strength of indirect SOC.

In conclusion, the electronic and magnetic properties were modulated by the biaxial strains of changing the occupation of Fe's d orbitals, as shown in Figure S13. A similar phenomenon appears in other low-dimensional materials with intrinsic ferromagnetism.³¹

4. CONCLUSIONS

In summary, we have predicted and researched the electromagnetic properties of FeI₃ ML. We have found controllable electromagnetic properties in FeI₃ ML with a T_c of 148 K by using particle-swarm search approaches and DFT. FeI₃ is HSC with a gap of 1.692 eV. FeI₃ shows an intrinsic FM order, and the ferromagnetism comes from the superexchange interaction of the Fe–I–Fe bonds with an angle close to 90° . The EA prefers PMA, and the MAE and MCA values were 3.19 meV and 1.15 erg/cm², respectively. The Young's modulus of FeI₃ was 35.6 GPa. The CB and VB of FeI₃ are composed of the in-plane atomic orbitals. The compressive biaxial strain could effectively modulate FeI₃ from the FM state to the AFM state. Meanwhile, FeI₃ transforms HSC to spin-unpolarized SC under a biaxial compressive strain of -4.7% . The FM order could be enhanced as the superexchange was enhanced when the tensile strain increased. Magnetic moment, ΔE , J , and T_c could be effectively controlled by the biaxial strains. The EA could be switched from in-plane to out-of-plane at the critical strain of -4.7% . The MCA energy also changes with the biaxial strains. Magnetic and electronic properties show a very strong in-plane strain dependence. It originates from changes in the relative occupation of Fe d orbitals. Our research presents FM FeI₃ ML with high T_c which could be controlled by biaxial strains, which implies wide potential applications in electro-magnetics.

■ ASSOCIATED CONTENT

Supporting Information

The Supporting Information is available free of charge at <https://pubs.acs.org/doi/10.1021/acsaelm.1c00363>.

Information on materials; parameters in CALYPSO; U -test on lattice; kinetic energy cutoff test; phonon spectrum test; PDOS; d-orbital projected-band structure; band structures with AFM orders; band structure with SOC; U -test on band structure; convergence test on MCA; MAE change with θ and φ of FeI₃ ML; phonon spectrum of CrI₃ and CrCl₃; orbital projected-band structure; IDOS under strains; band structure and PDOS of FeCl₃, FeBr₃, and FeI₃; geometry of stacking order; and PDOS of stacking order (PDF)

■ AUTHOR INFORMATION

Corresponding Author

Zhaoyong Guan – Key Laboratory of Colloid and Interface Chemistry, Ministry of Education, School of Chemistry and Chemical Engineering, Shandong University, Jinan, Shandong 250100, P. R. China; Science Center for Material Creation and Energy Conversion, School of Chemistry and Chemical Engineering, Shandong University, Jinan, Shandong 250100, P.R. China; orcid.org/0000-0002-4103-6507; Phone: +86-0531-88363179; Email: zyguan@sdu.edu.cn

Author

Shuang Ni – Research Center of Laser Fusion, China Academy of Engineering Physics, Mianyang, Sichuan 621900, P. R. China

Complete contact information is available at:

<https://pubs.acs.org/10.1021/acsaelm.1c00363>

Notes

The authors declare no competing financial interest.

■ ACKNOWLEDGMENTS

The authors thank Prof. Xingxing Li for discussion of calculations of Curie temperature, Prof. Liang Ma, Shuqing Zhang, and Chunmei Zhang for calculations of MCA, Dr. Haidi Wang for calculations of Young's modulus, Prof. Bing Wang for experimental realization of strains, Dr. Yizhou Liu for 3D plots of MAE using MATLAB, Prof. Chengxi Huang and Fawei Zheng for calculations of exchange interactions. This work was supported by the financial support from the Natural Science Foundation of China (Grant no. 11904203) and the Fundamental Research Funds of Shandong University (Grant no. 2019GN065). The scientific calculations in this paper have been done on the HPC Cloud Platform of Shandong University. The authors also acknowledge the Beijing Super Cloud Computing Center (BSCC) and Shanghai Super-computer Center for providing HPC resources.

■ REFERENCES

- (1) Geim, A. K.; Novoselov, K. S. The Rise of Graphene. *Nat. Mater.* **2007**, *6*, 183–191.
- (2) Castro Neto, A. H.; Guinea, F.; Peres, N. M. R.; Novoselov, K. S.; Geim, A. K. The Electronic Properties of Graphene. *Rev. Mod. Phys.* **2009**, *81*, 109–162.
- (3) Guan, Z.; Si, C.; Hu, S.; Duan, W. First-Principles Study of Line-Defect-Embedded Zigzag Graphene Nanoribbons: Electronic and Magnetic Properties. *Phys. Chem. Chem. Phys.* **2016**, *18*, 12350–12356.
- (4) Guan, Z.; Ni, S. Predicted 2D Ferromagnetic Janus VSeTe Monolayer with High Curie Temperature, Large Valley Polarization and Magnetic Crystal Anisotropy. *Nanoscale* **2020**, *12*, 22735–22742.
- (5) Guan, Z.; Luo, N.; Ni, S.; Hu, S. Tunable Electronic and Magnetic Properties of Monolayer and Bilayer Janus Cr₂Cl₃I₃: A First-Principles Study. *Mater. Adv.* **2020**, *1*, 244–253.
- (6) Guan, Z.; Ni, S.; Hu, S. Band Gap Opening of Graphene by Forming a Graphene/PtSe₂ Van Der Waals Heterojunction. *RSC Adv.* **2017**, *7*, 45393–45399.
- (7) Guan, Z.; Ni, S.; Hu, S. Tuning the Electronic and Magnetic Properties of Graphene Flake Embedded in Boron Nitride Nanoribbons with Transverse Electric Fields: First-Principles Calculations. *ACS Omega* **2019**, *4*, 10293–10301.
- (8) Guan, Z.; Lian, C.-S.; Hu, S.; Ni, S.; Li, J.; Duan, W. Tunable Structural, Electronic, and Optical Properties of Layered Two-Dimensional C₂N and MoS₂ Van Der Waals Heterostructure as Photovoltaic Material. *J. Phys. Chem. C* **2017**, *121*, 3654–3660.

- (9) Guan, Z.; Ni, S.; Hu, S. Tunable Electronic and Optical Properties of Monolayer and Multilayer Janus MoSSe as a Photocatalyst for Solar Water Splitting: A First-Principles Study. *J. Phys. Chem. C* **2018**, *122*, 6209–6216.
- (10) Wang, Q. H.; Kalantar-Zadeh, K.; Kis, A.; Coleman, J. N.; Strano, M. S. Electronics and Optoelectronics of Two-Dimensional Transition Metal Dichalcogenides. *Nat. Nanotechnol.* **2012**, *7*, 699–712.
- (11) Liu, H.; Neal, A. T.; Zhu, Z.; Luo, Z.; Xu, X.; Tománek, D.; Ye, P. D. Phosphorene: An Unexplored 2D Semiconductor with a High Hole Mobility. *ACS Nano* **2014**, *8*, 4033–4041.
- (12) Novoselov, K. S.; Mishchenko, A.; Carvalho, A.; Castro Neto, A. H. 2D Materials and Van Der Waals Heterostructures. *Science* **2016**, *353*, aac9439.
- (13) Mermin, N. D.; Wagner, H. Absence of Ferromagnetism or Antiferromagnetism in One- or Two-Dimensional Isotropic Heisenberg Models. *Phys. Rev. Lett.* **1966**, *17*, 1133–1136.
- (14) Sun, Z.; Yi, Y.; Song, T.; Clark, G.; Huang, B.; Shan, Y.; Wu, S.; Huang, D.; Gao, C.; Chen, Z.; McGuire, M.; Cao, T.; Xiao, D.; Liu, W.-T.; Yao, W.; Xu, X.; Wu, S. Giant Nonreciprocal Second-Harmonic Generation from Antiferromagnetic Bilayer CrI₃. *Nature* **2019**, *572*, 497–501.
- (15) Song, T.; Cai, X.; Tu, M. W.-Y.; Zhang, X.; Huang, B.; Wilson, N. P.; Seyler, K. L.; Zhu, L.; Taniguchi, T.; Watanabe, K.; McGuire, M. A.; Cobden, D. H.; Xiao, D.; Yao, W.; Xu, X. Giant Tunneling Magnetoresistance in Spin-Filter Van Der Waals Heterostructures. *Science* **2018**, *360*, 1214–1218.
- (16) Huang, B.; Clark, G.; Navarro-Moratalla, E.; Klein, D. R.; Cheng, R.; Seyler, K. L.; Zhong, D.; Schmidgall, E.; McGuire, M. A.; Cobden, D. H.; Yao, W.; Xiao, D.; Jarillo-Herrero, P.; Xu, X. Layer-Dependent Ferromagnetism in a Van Der Waals Crystal Down to the Monolayer Limit. *Nature* **2017**, *546*, 270.
- (17) Gong, C.; Li, L.; Li, Z.; Ji, H.; Stern, A.; Xia, Y.; Cao, T.; Bao, W.; Wang, C.; Wang, Y.; Qiu, Z. Q.; Cava, R. J.; Louie, S. G.; Xia, J.; Zhang, X. Discovery of Intrinsic Ferromagnetism in Two-Dimensional Van Der Waals Crystals. *Nature* **2017**, *546*, 265.
- (18) Gibertini, M.; Koperski, M.; Morpurgo, A. F.; Novoselov, K. S. Magnetic 2D Materials and Heterostructures. *Nat. Nanotechnol.* **2019**, *14*, 408–419.
- (19) Bonilla, M.; Kolekar, S.; Ma, Y.; Diaz, H. C.; Kalappattil, V.; Das, R.; Eggers, T.; Gutierrez, H. R.; Phan, M.-H.; Batzill, M. Strong Room-Temperature Ferromagnetism in VSe₂ Monolayers on Van Der Waals Substrates. *Nat. Nanotechnol.* **2018**, *13*, 289–293.
- (20) Wang, N.; Tang, H.; Shi, M.; Zhang, H.; Zhuo, W.; Liu, D.; Meng, F.; Ma, L.; Ying, J.; Zou, L.; Sun, Z.; Chen, X. Transition from Ferromagnetic Semiconductor to Ferromagnetic Metal with Enhanced Curie Temperature in Cr₂Ge₂Te₆ Via Organic Ion Intercalation. *J. Am. Chem. Soc.* **2019**, *141*, 17166–17173.
- (21) Verzhbitskiy, I. A.; Kurebayashi, H.; Cheng, H.; Zhou, J.; Khan, S.; Feng, Y. P.; Eda, G. Controlling the Magnetic Anisotropy in Cr₂Ge₂Te₆ by Electrostatic Gating. *Nat. Electron.* **2020**, *3*, 460–465.
- (22) Chen, W.; Sun, Z.; Wang, Z.; Gu, L.; Xu, X.; Wu, S.; Gao, C. Direct Observation of Van Der Waals Stacking-Dependent Interlayer Magnetism. *Science* **2019**, *366*, 983–987.
- (23) Huang, B.; Clark, G.; Klein, D. R.; MacNeill, D.; Navarro-Moratalla, E.; Seyler, K. L.; Wilson, N.; McGuire, M. A.; Cobden, D. H.; Xiao, D.; Yao, W.; Jarillo-Herrero, P.; Xu, X. Electrical Control of 2D Magnetism in Bilayer CrI₃. *Nat. Nanotechnol.* **2018**, *13*, 544–548.
- (24) Deng, Y.; Yu, Y.; Song, Y.; Zhang, J.; Wang, N. Z.; Sun, Z.; Yi, Y.; Wu, Y. Z.; Wu, S.; Zhu, J.; Wang, J.; Chen, X. H.; Zhang, Y. Gate-Tunable Room-Temperature Ferromagnetism in Two-Dimensional Fe₃GeTe₂. *Nature* **2018**, *563*, 94–99.
- (25) Li, X.; Lü, J.-T.; Zhang, J.; You, L.; Su, Y.; Tsymbal, E. Y. Spin-Dependent Transport in Van Der Waals Magnetic Tunnel Junctions with Fe₃GeTe₂ Electrodes. *Nano Lett.* **2019**, *19*, 5133–5139.
- (26) Verchenko, V. Y.; Tsirlin, A. A.; Sobolev, A. V.; Presniakov, I. A.; Shevelkov, A. V. Ferromagnetic Order, Strong Magnetocrystalline Anisotropy, and Magnetocaloric Effect in the Layered Telluride Fe_{3-δ}GeTe₂. *Inorg. Chem.* **2015**, *54*, 8598–8607.
- (27) Zhuang, H. L.; Kent, P. R. C.; Hennig, R. G. Strong Anisotropy and Magnetostriction in the Two-Dimensional Stoner Ferromagnet Fe₃GeTe₂. *Phys. Rev. B* **2016**, *93*, 134407.
- (28) Li, H.; Ruan, S.; Zeng, Y. J. Intrinsic Van Der Waals Magnetic Materials from Bulk to the 2D Limit: New Frontiers of Spintronics. *Adv. Mater.* **2019**, *31*, 1900065–1900099.
- (29) Niu, B.; Su, T.; Francisco, B. A.; Ghosh, S.; Kargar, F.; Huang, X.; Lohmann, M.; Li, J.; Xu, Y.; Taniguchi, T.; Watanabe, K.; Wu, D.; Balandin, A.; Shi, J.; Cui, Y.-T. Coexistence of Magnetic Orders in Two-Dimensional Magnet CrI₃. *Nano Lett.* **2020**, *20*, 553–558.
- (30) Morell, E. S.; León, A.; Miwa, R. H.; Vargas, P. Control of Magnetism in Bilayer CrI₃ by an External Electric Field. *2D Materials* **2019**, *6*, 025020–025025.
- (31) Guan, Z.; Ni, S. Strain-Controllable High Curie Temperature, Large Valley Polarization, and Magnetic Crystal Anisotropy in a 2D Ferromagnetic Janus VSeTe Monolayer. *ACS Appl. Mater. Interfaces* **2020**, *12*, 53067–53075.
- (32) Zheng, F.; Zhao, J.; Liu, Z.; Li, M.; Zhou, M.; Zhang, S.; Zhang, P. Tunable Spin States in the Two-Dimensional Magnet CrI₃. *Nanoscale* **2018**, *10*, 14298–14303.
- (33) Klein, D. R.; MacNeill, D.; Song, Q.; Larson, D. T.; Fang, S.; Xu, M.; Ribeiro, R. A.; Canfield, P. C.; Kaxiras, E.; Comin, R.; Jarillo-Herrero, P. Enhancement of Interlayer Exchange in an Ultrathin Two-Dimensional Magnet. *Nat. Phys.* **2019**, *15*, 1255–1260.
- (34) Sivasdas, N.; Okamoto, S.; Xu, X.; Fennie, C. J.; Xiao, D. Stacking-Dependent Magnetism in Bilayer CrI₃. *Nano Lett.* **2018**, *18*, 7658–7664.
- (35) Cai, X.; Song, T.; Wilson, N. P.; Clark, G.; He, M.; Zhang, X.; Taniguchi, T.; Watanabe, K.; Yao, W.; Xiao, D.; McGuire, M. A.; Cobden, D. H.; Xu, X. Atomically Thin CrCl₃: An in-Plane Layered Antiferromagnetic Insulator. *Nano Lett.* **2019**, *19*, 3993–3998.
- (36) Burch, K. S. Electric Switching of Magnetism in 2D. *Nat. Nanotechnol.* **2018**, *13*, 532.
- (37) Liu, Z.; Guo, K.; Hu, G.; Shi, Z.; Li, Y.; Zhang, L.; Chen, H.; Zhang, L.; Zhou, P.; Lu, H.; Lin, M.-L.; Liu, S.; Cheng, Y.; Liu, X. L.; Xie, J.; Bi, L.; Tan, P.-H.; Deng, L.; Qiu, C.-W.; Peng, B. Observation of Nonreciprocal Magnetophonon Effect in Nonencapsulated Few-Layered CrI₃. *Sci. Adv.* **2020**, *6*, No. eabc7628.
- (38) Ghazaryan, D.; Greenaway, M. T.; Wang, Z.; Guarochico-Moreira, V. H.; Vera-Marun, I. J.; Yin, J.; Liao, Y.; Morozov, S. V.; Kristanovski, O.; Lichtenstein, A. I.; Katsnelson, M. I.; Withers, F.; Mishchenko, A.; Eaves, L.; Geim, A. K.; Novoselov, K. S.; Misra, A. Magnon-Assisted Tunnelling in Van Der Waals Heterostructures Based on CrBr₃. *Nat. Electron.* **2018**, *1*, 344–349.
- (39) Wu, Z.; Yu, J.; Yuan, S. Strain-Tunable Magnetic and Electronic Properties of Monolayer CrI₃. *Phys. Chem. Chem. Phys.* **2019**, *21*, 7750–7755.
- (40) Gao, Y.; Wang, J.; Li, Z.; Yang, J.; Xia, M.; Hao, X.; Xu, Y.; Gao, F. On the Ferromagnetism and Band Tailoring of CrI₃ Single Layer. *Phys. Status Solidi RRL* **2019**, *13*, 1800410.
- (41) Dolui, K.; Petrović, M. D.; Zollner, K.; Plecháč, P.; Fabian, J.; Nikolić, B. K. Proximity Spin–Orbit Torque on a Two-Dimensional Magnet within Van Der Waals Heterostructure: Current-Driven Antiferromagnet-to-Ferromagnet Reversible Nonequilibrium Phase Transition in Bilayer CrI₃. *Nano Lett.* **2020**, *20*, 2288–2295.
- (42) Zhong, D.; Seyler, K. L.; Linpeng, X.; Cheng, R.; Sivasdas, N.; Huang, B.; Schmidgall, E.; Taniguchi, T.; Watanabe, K.; McGuire, M. A.; Yao, W.; Xiao, D.; Fu, K.-M. C.; Xu, X. Van Der Waals Engineering of Ferromagnetic Semiconductor Heterostructures for Spin and Valleytronics. *Sci. Adv.* **2017**, *3*, No. e1603113.
- (43) Hou, Y.; Kim, J.; Wu, R. Magnetizing Topological Surface States of Bi₂Se₃ with a CrI₃ Monolayer. *Sci. Adv.* **2019**, *5*, No. eaaw1874.
- (44) Lu, M.; Yao, Q.; Li, Q.; Xiao, C.; Huang, C.; Kan, E. Tuning Electronic and Magnetic Properties of Two-Dimensional Ferromagnetic Semiconductor CrI₃ through Adsorption of Benzene. *J. Phys. Chem. C* **2020**, *124*, 22143–22149.
- (45) Rassekh, M.; He, J.; Farjami Shayesteh, S.; Palacios, J. J. Remarkably Enhanced Curie Temperature in Monolayer CrI₃ by

Hydrogen and Oxygen Adsorption: A First-Principles Calculations. *Comput. Mater. Sci.* **2020**, *183*, 109820.

(46) Webster, L.; Yan, J.-A. Strain-Tunable Magnetic Anisotropy in Monolayer CrCl_3 , CrBr_3 , and CrI_3 . *Phys. Rev. B* **2018**, *98*, 144411–144418.

(47) Kvashnin, Y. O.; Bergman, A.; Lichtenstein, A. I.; Katsnelson, M. I. Relativistic Exchange Interactions in CrX_3 ($X = \text{Cl}, \text{Br}, \text{I}$) Monolayers. *Phys. Rev. B* **2020**, *102*, 115162–115172.

(48) Kresse, G.; Furthmüller, J. Efficiency of Ab-Initio Total Energy Calculations for Metals and Semiconductors Using a Plane-Wave Basis Set. *Comput. Mater. Sci.* **1996**, *6*, 15–50.

(49) Perdew, J. P.; Burke, K.; Ernzerhof, M. Generalized Gradient Approximation Made Simple. *Phys. Rev. Lett.* **1996**, *77*, 3865–3868.

(50) Heyd, J.; Scuseria, G. E.; Ernzerhof, M. Hybrid Functionals Based on a Screened Coulomb Potential. *J. Chem. Phys.* **2003**, *118*, 8207–8215.

(51) Heyd, J.; Scuseria, G. E.; Ernzerhof, M. Erratum: “Hybrid Functionals Based on a Screened Coulomb Potential” [*J. Chem. Phys.* **118**, 8207 (2003)]. *J. Chem. Phys.* **2006**, *124*, 219906.

(52) Liechtenstein, A. I.; Anisimov, V. I.; Zaanen, J. Density-Functional Theory and Strong Interactions: Orbital Ordering in Mott-Hubbard Insulators. *Phys. Rev. B: Condens. Matter Mater. Phys.* **1995**, *52*, R5467–R5470.

(53) Grimme, S. Semiempirical GGA-Type Density Functional Constructed with a Long-Range Dispersion Correction. *J. Comput. Chem.* **2006**, *27*, 1787–1799.

(54) Togo, A.; Tanaka, I. First Principles Phonon Calculations in Materials Science. *Scripta Mater.* **2015**, *108*, 1–5.

(55) Nosé, S. A Unified Formulation of the Constant Temperature Molecular Dynamics Methods. *J. Chem. Phys.* **1984**, *81*, 511–519.

(56) Wang, Y.; Lv, J.; Zhu, L.; Ma, Y. Crystal Structure Prediction Via Particle-Swarm Optimization. *Phys. Rev. B: Condens. Matter Mater. Phys.* **2010**, *82*, 094116.

(57) Henkelman, G.; Arnaldsson, A.; Jónsson, H. A Fast and Robust Algorithm for Bader Decomposition of Charge Density. *Comput. Mater. Sci.* **2006**, *36*, 354–360.

(58) Anderson, P. W. Antiferromagnetism. Theory of Superexchange Interaction. *Phys. Rev.* **1950**, *79*, 350–356.

(59) Goodenough, J. B. Theory of the Role of Covalence in the Perovskite-Type Manganites $[\text{La}, \text{M}(\text{II})]\text{MnO}_3$. *Phys. Rev.* **1955**, *100*, 564–573.

(60) Kanamori, J. Superexchange Interaction and Symmetry Properties of Electron Orbitals. *J. Phys. Chem. Solids* **1959**, *10*, 87–98.

(61) Huang, C.; Feng, J.; Wu, F.; Ahmed, D.; Huang, B.; Xiang, H.; Deng, K.; Kan, E. Toward Intrinsic Room-Temperature Ferromagnetism in Two-Dimensional Semiconductors. *J. Am. Chem. Soc.* **2018**, *140*, 11519–11525.

(62) Xiang, H. J.; Wei, S.-H.; Whangbo, M.-H. Origin of the Structural and Magnetic Anomalies of the Layered Compound SrFeO_2 : A Density Functional Investigation. *Phys. Rev. Lett.* **2008**, *100*, 167207.

(63) Bogdanov, A. N.; Dragunov, I. E. Metastable States, Spin-Reorientation Transitions, and Domain Structures in Planar Hexagonal Antiferromagnets. *Low Temp. Phys.* **1998**, *24*, 852–857.

(64) Zhuang, H. L.; Hennig, R. G. Stability and Magnetism of Strongly Correlated Single-Layer VS_2 . *Phys. Rev. B* **2016**, *93*, 054429.

(65) Lado, J. L.; Fernández-Rossier, J. On the Origin of Magnetic Anisotropy in Two Dimensional CrI_3 . *2D Materials* **2017**, *4*, 035002.

(66) Wang, D.-s.; Wu, R.; Freeman, A. J. First-Principles Theory of Surface Magnetocrystalline Anisotropy and the Diatomic-Pair Model. *Phys. Rev. B: Condens. Matter Mater. Phys.* **1993**, *47*, 14932–14947.

(67) Wang, H.; Li, X.; Li, P.; Yang, J. δ -Phosphorene: A Two Dimensional Material with a Highly Negative Poisson's Ratio. *Nanoscale* **2017**, *9*, 850–855.

(68) Zhang, W.-B.; Qu, Q.; Zhu, P.; Lam, C.-H. Robust Intrinsic Ferromagnetism and Half Semiconductivity in Stable Two-Dimensional Single-Layer Chromium Trihalides. *J. Mater. Chem. C* **2015**, *3*, 12457–12468.

(69) Bertolazzi, S.; Brivio, J.; Kis, A. Stretching and Breaking of Ultrathin MoS_2 . *ACS Nano* **2011**, *5*, 9703–9709.

(70) Booth, T. J.; Blake, P.; Nair, R. R.; Jiang, D.; Hill, E. W.; Bangert, U.; Bleloch, A.; Gass, M.; Novoselov, K. S.; Katsnelson, M. I.; Geim, A. K. Macroscopic Graphene Membranes and Their Extraordinary Stiffness. *Nano Lett.* **2008**, *8*, 2442–2446.